Nanoscale

PAPER

View Article Online
View Journal | View Issue

Cite this: *Nanoscale*, 2022, **14**, 9359

Photoconductive focal plane array based on HgTe quantum dots for fast and cost-effective short-wave infrared imaging†

Charlie Gréboval,[a] David Darson,[b] Victor Parahyba,[c] Rodolphe Alchaar,[a] Claire Abadie,[d] Vincent Noguier,[c] Simon Ferré,[c] Eva Izquierdo,[a] Adrien Khalili,[a] Yoann Prado,[a] Pierre Potet[c] and Emmanuel Lhuillier *[a]

HgTe nanocrystals, thanks to quantum confinement, present a broadly tunable band gap all over the infrared spectral range. In addition, significant efforts have been dedicated to the design of infrared sensors with an absorbing layer made of nanocrystals. However, most efforts have been focused on single pixel sensors. Nanocrystals offer an appealing alternative to epitaxially grown semiconductors for infrared imaging by reducing the material growth cost and easing the coupling to the readout circuit. Here we propose a strategy to design an infrared focal plane array from a single fabrication step. The focal plane array (FPA) relies on a specifically designed readout circuit enabling in plane electric field application and operation in photoconductive mode. We demonstrate a VGA format focal plane array with a 15 μm pixel pitch presenting an external quantum efficiency of 4–5% (15% internal quantum efficiency) for a cut-off around 1.8 μm and operation using Peltier cooling only. The FPA is compatible with 200 fps imaging full frame and imaging up to 340 fps is demonstrated by driving a reduced area of the FPA. In the last part of the paper, we discuss the cost of such sensors and show that the latter is only driven by labor costs while we estimate the cost of the NC film to be in the 10–20 € range.

Received 7th March 2022,
Accepted 10th June 2022

DOI: 10.1039/d2nr01313d

rsc.li/nanoscale

Introduction

Infrared (IR) sensing is driven by epitaxially grown semiconductors such as InGaAs for the short-wave infrared (SWIR), InSb and HgCdTe for the mid-wave infrared (MWIR) and mostly HgCdTe in the long-wave infrared (LWIR). Heterostructures of III–V semiconductors, the so-called quantum well infrared photodetectors (QWIP) and type-II superlattices complete the family of quantum detectors in this spectral range. In all cases, the material growth accounts for a significant part of the focal plane array (FPA) final cost. In addition, the coupling of this active layer to the readout integrated circuit (ROIC) is complex. In general, indium bumps ensure the electrical coupling between the absorbing semiconductor and the ROIC. This step adds cost, reduces the production yield, and complicates the pixel size reduction, although pixel pitches close to the diffraction limit provide higher image quality.[1] Because these technologies are already established, their roadmaps do not offer a clear route to substantial cost reduction. Therefore, new materials have to be considered. In the short and mid wave infrared, the strong vibrations occurring in conductive polymers prevent their use as light sensors. Colloidal quantum dots (QDs) now offer an interesting alternative.[2] Over the past two decades, a lot of efforts have been dedicated, first to push their absorption toward longer wavelengths[3–5] and later to integrate them into functional devices such as LEDs,[6–9] solar cells[10] and IR sensors.[2,11–14] For the latter application, most of the efforts

[a]*Sorbonne Université, CNRS, Institut des NanoSciences de Paris, INSP, F-75005 Paris, France. E-mail: el@insp.upmc.fr*
[b]*Laboratoire de Physique de l'Ecole normale supérieure, ENS, Université PSL, CNRS, Sorbonne Université, Université Paris-Diderot, Sorbonne Paris Cité, Paris, France*
[c]*New Imaging Technologies SA, 1 impasse de la Noisette, 91370 Verrières le Buisson, France*
[d]*ONERA – The French Aerospace Lab, 6, chemin de la Vauve aux Granges, BP 80100 91123 Palaiseau, France*

† Electronic supplementary information (ESI) available: Ellipsometric measurements, simulation of the electric field and current density distribution, additional data relative to EQE determination, imaging at high frame rate, procedure for image correction, additional infrared imaging using band pass filters. We also provide four videos. Video S1 depicts a living scene that is taken while the sun is the only light source. Video S2 depicts the same series of vials containing solvents as shown in Fig. 5a, while the Si wafer/ITO substrate are moved in front of the scene. Video S3 depicts the same series of vials containing solvents as shown in Fig. 5a, while a soldering iron (at 400 °C) is moved in front to show passive imaging of warm objects. Video S4 shows the high frame rate imaging of a chopper wheel while the chopper is in phase or out of phase with respect to the acquisition of the FPA. See DOI: https://doi.org/10.1039/d2nr01313d

have been focused on the design of single pixel devices, but there are few reports relative to image sensors.[12,15–19] Several companies (such as SWIR Vision,[20–22] ST Microelectronics,[23] IMEC,[1,24–26] Emberion,[27] QDIR, Osram) are now developing or even commercializing nanocrystal-based cameras.

The majority of the attention has been drawn to two materials: PbS and HgTe. Lead sulfide has initially been developed as a material for solar cells.[28] Its band gap can easily be tuned to match the optimal value for single junction solar cells. In addition, the observation of multi exciton generation[29] at moderate pump energies has been seen as a path to overcome the Shockley–Queisser limitation. This widespread application has resulted in a large amount of work spent on this material, both on the material side to improve stability, doping control and carrier mobilities[30] and on the device side to design optimized photodiodes.[31,32] Alternatively, HgTe is a gap-less semiconductor in bulk form, allowing to explore absorption at wavelengths beyond the PbS band gap, especially in the MWIR. Significant progresses have also been made for this material integration, including demonstration of multicolor sensors,[33,34] coupling to light resonators,[35–39] or high carrier mobility films.[40] When it comes to focal plane arrays (FPAs), most efforts have so far been focused on a vertical geometry, which requires a multilayer deposition. Moreover, photodiode stacks have received far less attention in the case of HgTe, and all reported diodes currently have a top metallic contact (*i.e.* non transparent) that hinders the coupling to a ROIC. Here, we explore a simpler planar geometry, thanks to a specifically designed readout circuit enabling in plane bias application. Furthermore, the device can be obtained in a single step of fabrication which opens the door to very low-cost infrared imaging setups.

Discussion and results

The material of interest is made of HgTe QDs, the latter are grown using a scaled-up version (×2.5 in quantity at constant concentration) of the Keuleyan's procedure.[41] The QDs are then processed under an ink form to cap them with short ligands[42] (here a combination of short thiols and $HgCl_2$ salt) making them charge conduction compatible. This process tends to redshift the absorption spectrum, see Fig. S1.† The particle size is chosen so that after ligand exchange the band-edge matches the one of InGaAs, as shown in Fig. 1a. According to transmission electron microscopy, the particles

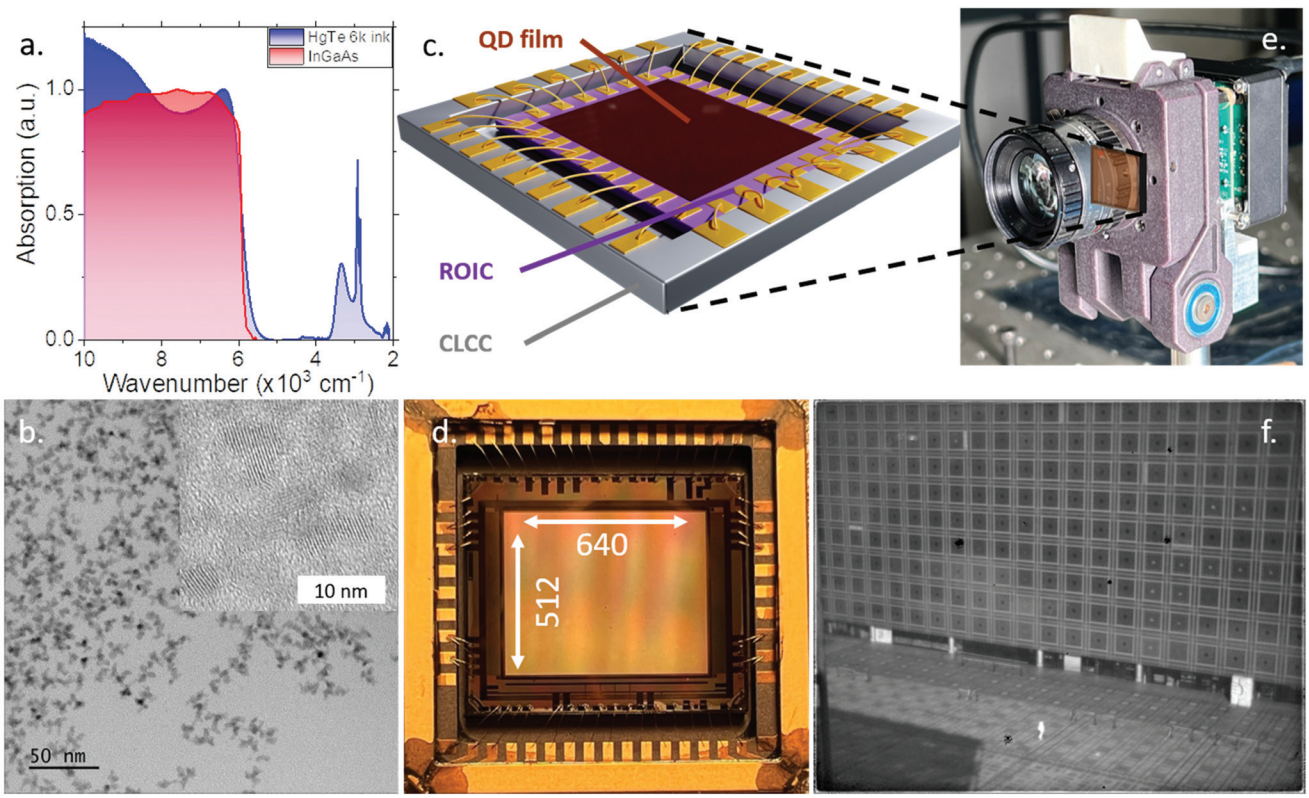

Fig. 1 Nanocrystal-based photoconductive ROIC. (a) Absorption spectra of HgTe QDs used in the quantum dot-based SWIR camera and a typical InGaAs photodetector. (b) TEM picture of HgTe QDs with a band edge at 6000 cm^{-1}. The particles have a tripodic shape and a size of 8 nm. The inset is a high-resolution image of the same particles. (c) Scheme of the device that is plugged in the camera based on a film of HgTe QDs. (d) Picture of the ROIC in the CLCC (ceramic lead less chip carrier) after deposition of the QD film. The 640 × 512 pixels matrix is represented with the white arrows. (e) Picture of the SWIR camera with a Computar M1614-SW objective. (f) Picture of a building (Arabic fine art museum of Paris) taken with the QD-based SWIR camera shown in part e.

have a branched aspect with a characteristic size in the 6–8 nm range, see Fig. 1b.

For the readout integrated circuit (ROIC), we use a modified version of the New Imaging Technologies (NIT) ROIC (model 1601 Quantum) allowing for bias application within the plane and presenting a flatter top surface compared to its regular version used to hybridize InGaAs photodiode arrays. The ROIC has a VGA format (640 × 512 pixels, see Fig. 1d) with a 15 μm pixel pitch. The ROIC is then fully packaged onto a ceramic and electronically connected to it through wire bonding, see Fig. 1c and d. To form an image at room temperature, this sensor is then introduced into a compact camera with a SWIR objective which couples the FPA to an electronic controller, see Fig. 1e. Our strategy enables the design of a camera from a single fabrication step. An image obtained from this camera operated at room temperature without a thermal management strategy is shown in Fig. 1f. The associated video is provided as video S1† and the lack of ghost effect should be noted.

To better reveal the operation of our FPA, we have conducted electromagnetic simulations to quantify the device absorption and electrostatic simulations to unveil the field and current mapping. We use an atomic force microscopy (AFM) image for the ROIC topology (Fig. 2a) as input to propose a model of the ROIC. The electrodes are made of a final top gold layer, while the surface is based on Si_3N_4 as the dielectric. The HgTe QD film thickness is in the 200–400 nm range depending on the ink concentration and the spin coating speed. The formed film is conformal to the substrate, see Fig. S2.†

As stated, the ROIC configuration enables to bias differently two consecutive pixels forming a checkerboard pattern, see the potential map in Fig. 2b as well as the static electric field and current density on Fig. S4.† The typical electric field is around ≈1 kV cm^{-1} with a limited inhomogeneity resulting from the tip effect in the vicinity of the electrodes. We have simulated the absorption spectrum of the FPA (see Fig. S1† for complex optical index used as input) and found that the absorption at the band edge reaches 30%, see Fig. 2d. Though the exact absorption localization, especially considering tip effects, can strongly depend on the exact geometry chosen to model the pixel, it appears that the absorption is mostly located on the top of the gold electrode, see Fig. 2c. The latter acts as a back-side mirror, allowing for a second pass of the light. This condition is ideal for charge collection in a QD film where the conduction is driven by hopping. Indeed, the short diffusion length resulting from the limited carrier mobility makes charge collection more efficient in the vicinity of the electrode.[42]

In the next stage, we quantified the FPA's dark current as a function of temperature and image integration time. For this purpose, a second camera environment has been built where FPA cooling is now possible thanks to a multi-stage Peltier, see Fig. S5.† The signal output of the camera is digitized over 16 bits. Fig. 3a shows the average charge count as a function of integration time for various temperatures in dark condition. At −4 °C, we notice a clear saturation of the dark counts that corresponds to the full filling of the pixel's capacitance. This limits the integration time below 10 ms. As the temperature is further reduced, the saturation regime shifts toward higher integration times (>200 ms for operation at −32 °C). We fit the thermal dependence of the dark current (slopes of Fig. 3a) with an Arrhenius law which assumes that the current magni-

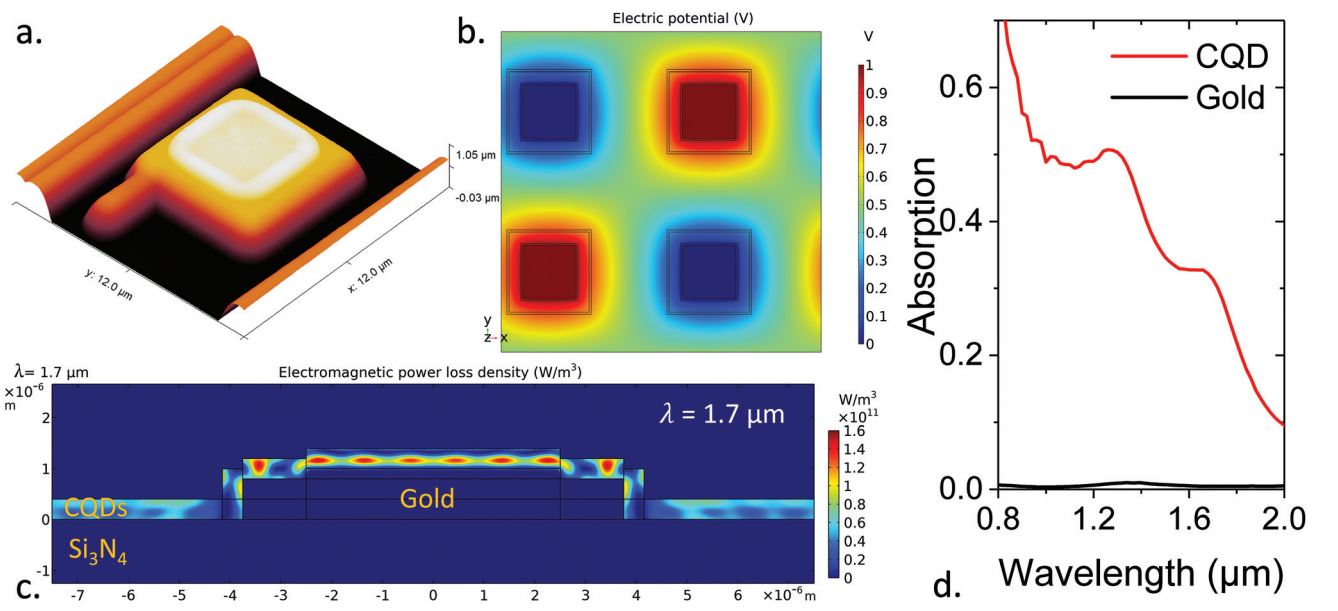

Fig. 2 Modeled optical and electrical properties of the ROIC. (a) Atomic force microscopy picture of one pixel from the ROIC before QD deposition. (b) Electric potential simulation of the ROIC whose pixels are biased to 0 and 1 V alternatively. (c) Electromagnetic absorption map at 1.7 μm of a pixel coated with a 400 nm HgTe QD film. (d) Simulated absorption spectrum integrated from the absorption map in b. In red the absorption in the QD film and in black the losses in the gold electrode.

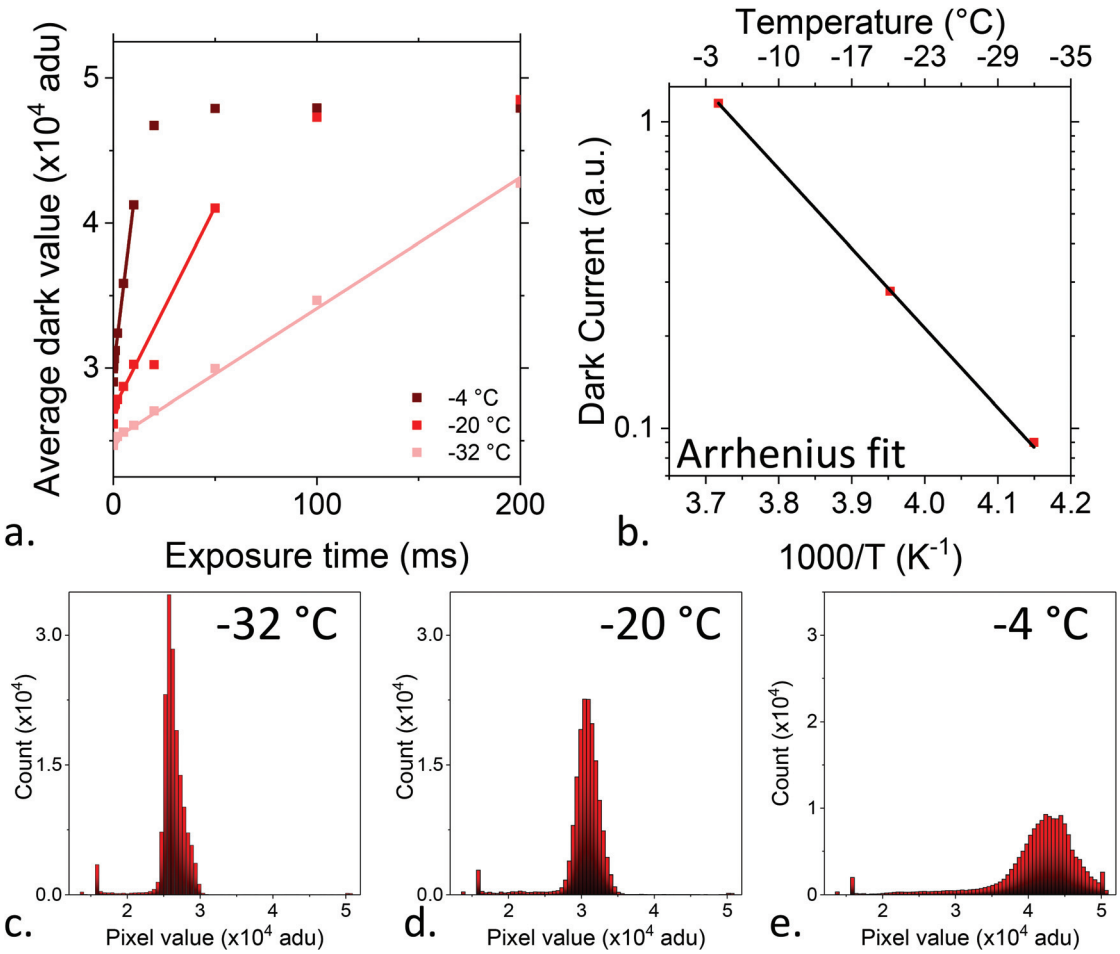

Fig. 3 Dark current conduction of the ROIC. (a) Average value of dark images as a function of exposure time for various temperatures. (b) Dark current decrease as a function of the cooling of the detector. The black line represents an Arrhenius exponential decay. Uncorrected histograms of dark images taken at −32 °C (c), −20 °C (d) and −4 °C (e) for a 10 ms exposure time.

tude is given by $I(T) = I_0 \cdot \exp(-E_a/k_b T)$, with E_a an activation energy, k_b the Boltzmann constant and T the temperature. We can extract an activation energy of 520 meV, see Fig. 3b. In other words, the dark current drops by one order of magnitude every 30 K, which is consistent with the observed shift of the time integration threshold to reach the ROIC capacitance full filling. This reduction of the average dark current is also well highlighted by the histogram of the charge counts for all the pixels of the FPA and an exposure time of 10 ms, see Fig. 3c. We can notice that not only lower temperatures reduce the average dark current but also the linewidth of the distribution.

We investigate the photocurrent signal coming from the FPA to quantify its external quantum efficiency (EQE). Using the following procedure, we measure for a given wavelength the number of charges within the ROIC capacitance as a function of the incident power, see Fig. 4a, S6 and 7.† We perform the same measurement using the same readout circuit coupled to an InGaAs photodiode array with a known absolute EQE (90% in our case), see Fig. S6.† We then compare the relative slope of the QD FPA and the InGaAs one to determine the absolute EQE of the former. We also have checked that the signal is linear as a function of the integration time up to 100 ms (operating temperature is −32 °C in this case, see Fig. 4c), that is the duration over which the capacitance is mostly fulfilled by the dark current as shown in Fig. 3. Obtained EQE values are reported in Fig. 4b and show typical EQE in the 4–5% range. Since the absorption of the band edge has been determined around 30%, the internal quantum efficiency is around 15%. This value is certainly modest compared to the best performing single pixel devices (with EQE reaching 80% for diodes[32] and even higher for devices with gain[43]). On the other hand, there are very few reported EQE values at the FPA level,[18] especially based on HgTe QDs. Buurma *et al.*[16] reported a 0.64% EQE, for a 320 × 256 pixel array with a 30 μm pixel pitch, but the cut-off wavelength was also much longer (5 μm) and operation was conducted at cryogenic temperature (100 K). The main reason for the modest EQE is the relatively large electrode spacing, which is highly detrimental in the case of hopping conduction. For PbS QD

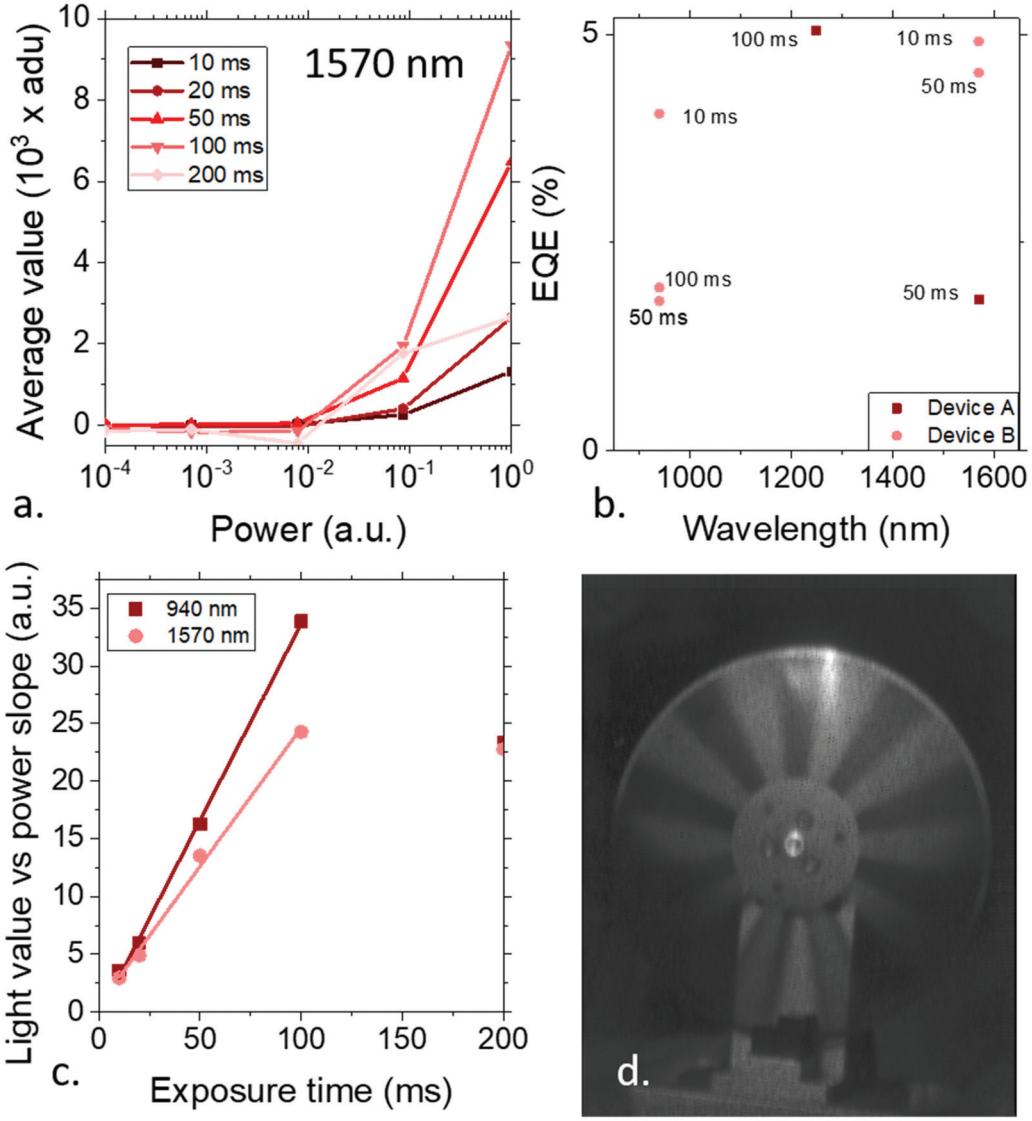

Fig. 4 Determination of the quantum efficiency and fast operation of the ROIC. (a) Average value (measured in analog digital units = magnitude of the digitalized number of electrons collected over 16 bits) of homogeneously illuminated pictures, taken at different relative powers in a 50 nm spectral range centred on 1570 nm for various exposure times and measured at −32 °C. (b) External quantum efficiencies of the HgTe QD camera as a function of the wavelength and the exposure time for two different devices. The external quantum efficiency is relative to the one of a 1601 InGaAs FPA from New Imaging Technologies. (c) Evolution of the detector response as a function of the exposure time at 940 nm and 1570 nm. The response is extracted from a linear fit of the average value as a function of the illumination power at −32 °C. (d) SWIR image of a chopper wheel at 170 Hz taken with the HgTe QD camera at −32 °C.

based FPAs, EQE have been reported up to 60% but at a shorter wavelength (1.4 μm cut-off wavelength[19,23,44,45]) and drop around 15% for a 2 μm cut-off[46] much closer to our device. It is important to stress that all these values based on PbS NCs rely on device geometries that are more complicated to fabricate than our single step FPA. The modest EQE compared to InGaAs certainly prevents the use of such sensor for applications with limited incident photon flux, however as our images prove it, it is already compatible with active imaging and industrial vision (trash sorting, detection of bruise of food...) applications.

The focal plane array can be operated full frame up to 200 frames per second (fps, see in Fig. 4d) and even faster operation can be achieved only selecting a part of the image. A video at 340 fps is proposed as Fig. S8 and video S4† on a 640 × 200 pixels region of interest.

In spite of its basic fabrication the sensor can image all over the NIR and SWIR range. Raw images are processed according to the procedure described in Fig. S9.† Basically, two reference images are collected respectively in the dark and under homogeneous illumination. The dark image will be used as offset, while the picture under illumination is used to

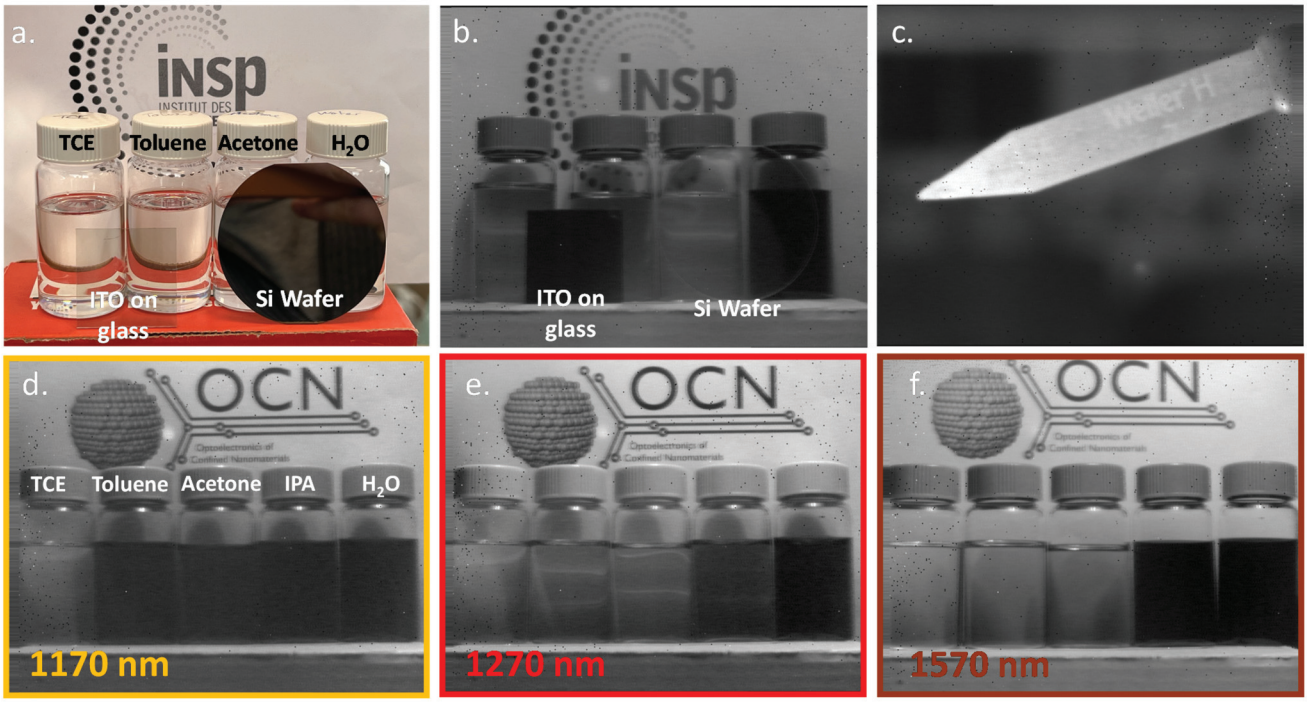

Fig. 5 SWIR imaging using HgTe QD-based FPA. (a) Visible picture (smartphone camera) of a scene with four vials containing from left to right: tetrachloroethylene (TCE), toluene, acetone and water (H_2O). In front of the vials, an ITO covered glass slide and a two inches silicon wafer are placed. (b) Same scene as in (a) taken with the HgTe QD based FPA. (c) Image of the tip of a soldering iron heated at 400 °C. (d–f) Scene composed of vials containing from left to right: TCE, toluene, acetone, isopropyl alcohol (IPA) and water imaged through a 1170 nm band pass filter (d), a 1270 nm bandpass filter (e) and a 1570 nm bandpass filter (f), all the SWIR pictures are taken through 50 nm spectral width bandpass filters and with an exposure time of 50 ms at −32 °C.

generate a gain map. All images are then treated using this procedure. Fig. 5 shows the imaging of vials containing various solvents transparent in the visible. To better highlight the change of contrast between visible and SWIR range, a visible transparent glass substrate coated with ITO (tin-doped indium oxide) and a reflective undoped Si wafer have been added to the front line, see Fig. 5a. As we switched to SWIR imaging using the QD based FPA, we can now see in Fig. 5b, S11 and video S2† through the Si wafer, while the water vial and the ITO/glass substrate now turn opaque. A more systematic study of the spectral dependence of this scene is shown in Fig. 5d–f and S10.† Blackbody radiation can also be detected using the HgTe QD-based sensor as revealed by the large contrast obtained by passively imaging the soldering iron, see Fig. 5c

To finish, we have tried to quantify the cost of such sensors (Table 1). For chemicals, we have used the cost charged at the laboratory level without considering any possible cost disruption relative to bulk ordering. Additional costs include amortization of the equipment, safety equipment, workforce. The cost of a nanocrystal growth has been estimated around 160 € per batch to obtain 16 mL of concentrated solution ([HgTe QD] ≈80 mg mL^{-1}). 77% of the growth cost actually relates to the workforce as it has been already pointed out in the case of QDs dedicated to solar cells.[47] This result further emphasizes the need for scaled up syntheses, since the time per synthesis is driving the final cost. As the QD solution is transformed into an ink, its value per liter increases by a factor ≈5 which mostly reflects the increase of concentration (×3.4) of the ink with respect to the pristine solution, now reaching 55 k€ per liter. To functionalize one ROIC, we use 30 μL of ink, meaning that 130 devices can be prepared for a batch of QD (4 mL of ink). The cost of the QD film on the ROIC has been estimated around 16 € per FPA, while the sensor cost is around 70 €. The former value has to be compared with the cost relative to InGaAs sensor estimated around 600 €. This highlights the potential of NC for cost reduction, particularly if scale effects (larger NC batches and wafer scale fabrication) start to be considered. For sure, this cost excludes amortization of research behind this development. It remains that the QD cost becomes a negligible part of the final camera, since for sake of comparison, the cost of a SWIR objective is around 500 €.

Certainly, the fact that the technology relies of Hg-based materials may also appears as an obvious limitation. But it should be pointed that the amount of HgTe per sensor is below 8 mg, while including the waste resulting from spin coating deposition. Further optimization of the deposition process, likely using inkjet[14] or spray[48] deposition, can further

Table 1 Costs associated with the different steps of fabrication of a QD-based sensor

Step	Cost	Amount	Cost for this step in €	Comment justification
QD colloidal growth	OLA	0.13 L	10.4	80 € L^{-1}
	TOP	5 mL	5	1000 € L^{-1}
	DDT	10 mL	0.2	20 € L^{-1}
	$HgCl_2$	1.36 g	0.9928	0.73 € g^{-1}
	Te	0.63 g	3.2949	5.23 € g^{-1}
	Alcohol	1 L	2	2 € L^{-1}
	Non-polar solvent	0.1 L	2.5	25 € L^{-1}
	Filter	1	1	1 € per filter
	Glassware	1	1.5	Schlenk line +50 € for 3 neck flask that can be used 100 times: 1.5 € per use
	Equipment	1	5	Balance, centrifuge, hood – 10k € amortization over 5 years, with 400 use per year: 5 € per use
	Workforce	2.5 hours	125	Assuming 70 k€ annual cost working 1500 hours a year: 50 € h^{-1}
	Safety	6 gloves	1.8	0.3 € per glove
	Pipette cone	6	3	0.5 € each
Cost per synthesis in €				**161.7**
Cost per L of QD solution in €				**10 105.5**
Ink preparation	$HgCl_2$	0.039 g	0.02847	0.73 € g^{-1}
	DMF	23.4 mL	0.234	10 € L^{-1}
	MpOH	2.6 mL	0.3276	126 € L^{-1}
	QD	16 mL	161.7	
	Safety	4	1.2	0.3 € per glove
	Pipette, cone	6	3	0.5 € each
	Workforce	1	50	Assuming 70 k€ annual cost working 1500 hours a year : 50€ h^{-1}
Cost per ink preparation in €				**216.5**
Cost per ink liter in €				**54 120**
Film deposition	QD film	30 μL	1.62	54 199.4 € L^{-1}
	Deposition	1	3	Spin coating + hood – 6000€ over 5 years; used 400 times a year: 3 € per use
	Pipette cones	6	3	0.5 € each
	Workforce	0.16 h	8.33	Assuming 70 k€ annual cost working 1500 hours a year: 50 € h^{-1}
	ROIC	1	6.62	1000 € for a 8 inches wafer sliced in 151 dies
	Packaging	1	50	Bonding, ceramic package…
QD cost per sensor in €				**≈16**
Cost per sensor in €				**≈73**

reduce this amount around 1 mg. It is thus important to notice that actual amount of toxic compound remains very low in such sensor.

Conclusion

We propose a strategy to build a cost-effective focal plane array based on QDs using a single step fabrication. The device relies on a ROIC that enables in plane electric field application and an absorbing layer made of HgTe QDs presenting a band gap similar to the one of InGaAs ($\lambda_{cut\text{-}off}$ = 1.7 μm). Homogeneous images over the VGA format array can be obtained and EQE reaches the 4–5% range for a device only cooled by a Peltier stage. In this condition, the FPA is operated in its linear regime and dark current is not prevailing as long as the integration time remains below 100 ms. Finally, we estimate the cost of such sensor and demonstrate that the overall cost is driven by labor costs, stressing the need for scaled-up syntheses that minimize manpower cost per mass of produced QDs. The cost of a film of QDs onto a ROIC has been determined in the 10–20 € range, for a ≈70 € cost per sensor, meaning that the active layer cost becomes almost negligible on the overall camera cost. This result raises new perspectives to broadly spread infrared sensor beyond the current niche market.

Methods

Chemicals

Mercury chloride ($HgCl_2$, Sigma-Aldrich, 99%), **mercury compounds are highly toxic. Handle them with special care.** Tellurium powder (Te, Sigma-Aldrich, 99.99%), trioctylphosphine (TOP, Alfa Aesar, 90%), oleylamine (OLA, Acros, 80–90%), dodecanethiol (DDT, Sigma-Aldrich, 98%), ethanol absolute anhydrous (VWR), methanol (VWR, >98%), isopropanol (IPA, VWR), hexane (VWR, 99%), octane (Carlo erba, 99%), 2-mercaptoethanol (MPOH, Merck, >99%), *N,N*-dimethylformamide (DMF, VWR), *N*-methylformamide (NMF, Alfa Aesar, 99%), toluene (VWR, 99.8%). All chemicals are used without further purification except oleylamine that is centrifuged before use.

1 M TOP:Te precursor

6.38 g of Te powder is mixed in 50 mL of TOP in a three neck flask. The flask is kept under vacuum at room temperature for

5 min and then the temperature is raised to 100 °C. Furthermore, degassing of flask is conducted for the next 20 min. The atmosphere is switched to nitrogen and the temperature is raised to 275 °C. The solution is stirred until a clear orange coloration is obtained. The flask is cooled down to room temperature and the color changes to yellow. Finally, this solution is transferred to a nitrogen filled glove box for storage.

HgTe NCs synthesis with band-edge at 6000 cm^{-1}

In a 250 mL three neck flask, 1360 mg of $HgCl_2$ (5 mmol) and 125 mL of oleylamine are degassed under vacuum at 110 °C. Meanwhile 5 mL of TOP:Te (1 M) are extracted from the glove box and mixed with 5 mL of oleylamine. After the atmosphere is switched to N_2 and the temperature stabilized at 56 °C, the TOP:Te solution is quickly injected. After 3 min, 10 mL of a mixture of DDT in toluene (25% of DDT) are injected and a water bath is used to quickly decrease the temperature. The content of the flask is split over 7 centrifugation tubes (50 mL) and MeOH is added (up to 40 mL). After centrifugation the formed pellet is redispersed in two centrifugation tubes with toluene. The solution is precipitated a second time with absolute EtOH (up to 40 mL). Again, the formed pellet is redispersed in toluene. At this step the nanocrystals are centrifuged in pure toluene to get rid of the lamellar phase. The solid phase is discarded. The stable phase is transferred in a vial after filtration (0.22 μm) with a volume of toluene V = 16 mL. The optical density of the NC solution is measured to be 0.32 at 400 nm after a 5000× dilution.

HgTe ink

16 mL of HgTe CQD solution in toluene (2.23 OD at 400 nm after a 500× dilution) is mixed with 26 mL of exchange solution containing 2.6 mL of DDT, 39 mg of $HgCl_2$ and 23.4 mL of DMF. Ligand exchange is performed for 3 min in a sonication bath. Then, the solution is precipitated by adding 40 mL of toluene and centrifuged at 6000 rpm for 3 min. Supernatant is discarded and the QDs are dried 10 min under vacuum before being redispersed in 4 mL of DMF. Finally, the ink is centrifuged 3 min at 6000 rpm and filtered through a 0.22 μm PTFE filter. The optical density of the ink is measured to be 0.92 at 400 nm after a 5000× dilution, which is roughly 3 times more concentrated than the initial solution.

For **infrared spectroscopy**, we use a Fischer Nicolet iS50 in attenuated total reflection (ATR) mode. The spectra are averaged over 32 acquisitions and have a 4 cm^{-1} resolution.

Transmission electron microscopy (TEM)

For TEM pictures, a drop of QD solution is drop-casted on a copper grid covered with an amorphous carbon film. The grid is degassed overnight under secondary vacuum. A JEOL 2010F is used at 200 kV for acquisition of pictures.

Spectroscopic ellipsometry

The spectroscopic ellipsometry measures the changes in the polarization state between the incident and the reflected light and is characterized by the angles ψ and Δ.

$$\rho = \frac{r_p}{r_s} = \left|\frac{r_p}{r_s}\right| e^{i(\delta_p - \delta_s)} = \tan\psi e^{i\Delta}$$

where r_p and r_s are the reflection coefficients of p and s polarized light respectively and where δ_p and δ_s are the phase shifts in reflection in p and s polarizations, respectively. The measurements are performed on a V-VASE ellipsometer (J. A. Woollam) in the 350–2500 nm range with steps of 10 nm and with angles of incidence of 55° and 65°.

Focal plane array fabrication

A ROIC packaged in a CLCC is cleaned in a O_2 plasma cleaner for 10 min. The ROIC is then placed on a spincoater and 30 μL of HgTe ink is spincoated at 1000 rpm and an acceleration of 500 rpm s^{-1} for 60 s and a drying step at 2000 rpm (1000 rpm s^{-1}) for 120 s. The film is further dried for 2 hours under primary vacuum.

Electromagnetic simulations are conducted using COMSOL, a software using Finite Element Method to solve Maxwell's equations. The array of resonators is modelled using RF module in 2D geometry. It is one unit cell and Floquet periodic boundary conditions are used to describe the periodicity. On both sides (top and bottom), we define perfectly matched layers (PML) to absorb all outgoing waves and prevent nonphysical reflections. The absorption calculated comes from the function "emw.Qe" which is the power density dissipated in W m^{-3}. On top of the resonator inside air, a port condition is used to define the incident wave, either in TE or TM polarization. This port is a periodic port where the orders of diffraction are automatically calculated by the software. A specific mesh is used for QD elements where the maximum element size is 20 nm. For all the rest, a predefined "Extremely fine" mesh is used, which means that the maximum element size is 210 nm and the minimum is 6 nm, except for the PML where a mapped mesh is used with a distribution of 12 elements. The inputs of the simulations are the refraction index of the materials which come from ellipsometry measurements for HgTe NCs (see Fig. S1†), from ref. 49 for gold and we use n = 2 and k = 0 for Si_3N_4,[50] where n is the refraction index and k the extinction coefficient.

Electrostatic simulations are also conducted using COMSOL. The array of resonators is modeled using AC/DC module in 3D geometry. Four electrodes are inside a unit cell and the periodic boundary conditions of the type "Continuity" are used. The main inputs of this simulation are the electrical conductivities, calculated experimentally for HgTe NCs (1.54×10^{-4} S m^{-1}), taken from COMSOL database for gold (44×10^6 S m^{-1}) and from ref. 51 for silicon nitride (1×10^{-13} S m^{-1}). The two other diagonal gold blocks are set to 0 V and the two other diagonals gold blocks are set to 1 V. The 4 borders are meshed identically side by side (with a copy face) to prevent any nonphysical asymmetry. For all the rest, a predefined "Extra fine" mesh is used, which means that the maximum element size is 1 μm and the minimum is 45 nm.

Author contributions

EL, VP, PP designed the project. VP, VN and SF designed the ROIC. CG, DD, VP, VN and SF conducted measurements. YP, CG and EI synthetized the nanocrystals. CG, EI and RA functionalized the ROIC. CA and AK conducted electromagnetic simulations. EL and CG wrote the manuscript with inputs and feedback from all authors.

Conflicts of interest

The authors declare no competing financial interest.

Acknowledgements

We thank Bruno Gallas for the use of ellipsometer and Herve Cruguel for conducting AFM measurements. The project is supported by ERC starting grant blackQD (grant no.756225). We acknowledge the use of clean-room facilities from the "Centrale de Proximité Paris-Centre". This work has been supported by the Region Ile-de-France in the framework of DIM Nano-K (grant dopQD). This work was supported by French state funds managed by the ANR within the Investissements d'Avenir programme under reference ANR-11-IDEX-0004-02, and more specifically within the framework of the Cluster of Excellence MATISSE and also by the grant IPER-Nano2 (ANR-18CE30-0023-01), Copin (ANR-19-CE24-0022), Frontal (ANR-19-CE09-0017), Graskop (ANR-19-CE09-0026), NITQuantum (ANR-20-ASTR-0008-01), Bright (ANR-21-CE24-0012-02) and MixDferro (ANR-21-CE09-0029).

References

1 J. Lee, E. Georgitzikis, Y. Li, Z. Lin, J. Park, I. Lieberman, D. Cheyns, M. Jayapala, A. Lambrechts, S. Thijs, R. Stahl and P. E. Malinowski, in *2020 IEEE International Electron Devices Meeting (IEDM)*, 2020, pp. 16.5.1–16.5.4.

2 T. Nakotte, S. G. Munyan, J. W. Murphy, S. A. Hawks, S. Kang, J. Han and A. M. Hiszpanski, *J. Mater. Chem. C*, 2022, **10**, 790–804.

3 S. Keuleyan, E. Lhuillier, V. Brajuskovic and P. Guyot-Sionnest, *Nat. Photonics*, 2011, **5**, 489–493.

4 N. Goubet, A. Jagtap, C. Livache, B. Martinez, H. Portalès, X. Z. Xu, R. P. S. M. Lobo, B. Dubertret and E. Lhuillier, *J. Am. Chem. Soc.*, 2018, **140**, 5033–5036.

5 M. V. Kovalenko, E. Kaufmann, D. Pachinger, J. Roither, M. Huber, J. Stangl, G. Hesser, F. Schäffler and W. Heiss, *J. Am. Chem. Soc.*, 2006, **128**, 3516–3517.

6 L. Bakueva, S. Musikhin, M. A. Hines, T.-W. F. Chang, M. Tzolov, G. D. Scholes and E. H. Sargent, *Appl. Phys. Lett.*, 2003, **82**, 2895–2897.

7 N. Tessler, V. Medvedev, M. Kazes, S. Kan and U. Banin, *Science*, 2002, **295**, 1506–1508.

8 J. Qu, M. Weis, E. Izquierdo, S. G. Mizrahi, A. Chu, C. Dabard, C. Gréboval, E. Bossavit, Y. Prado, E. Péronne, S. Ithurria, G. Patriarche, M. G. Silly, G. Vincent, D. Boschetto and E. Lhuillier, *Nat. Photonics*, 2022, **16**, 38–44.

9 J. Lim, Y. S. Park and V. I. Klimov, *Nat. Mater.*, 2018, **17**, 42–48.

10 G. H. Carey, A. L. Abdelhady, Z. Ning, S. M. Thon, O. M. Bakr and E. H. Sargent, *Chem. Rev.*, 2015, **115**, 12732–12763.

11 S. B. Hafiz, M. Scimeca, A. Sahu and D.-K. Ko, *Nano Converg.*, 2019, **6**, 7.

12 T. Rauch, M. Böberl, S. F. Tedde, J. Fürst, M. V. Kovalenko, G. Hesser, U. Lemmer, W. Heiss and O. Hayden, *Nat. Photonics*, 2009, **3**, 332–336.

13 S. A. McDonald, G. Konstantatos, S. Zhang, P. W. Cyr, E. J. D. Klem, L. Levina and E. H. Sargent, *Nat. Mater.*, 2005, **4**, 138–142.

14 M. Böberl, M. V. Kovalenko, S. Gamerith, E. J. W. List and W. Heiss, *Adv. Mater.*, 2007, **19**, 3574–3578.

15 A. J. Ciani, R. E. Pimpinella, C. H. Grein and P. Guyot-Sionnest, in *Infrared Technology and Applications XLII, International Society for Optics and Photonics*, 2016, vol. 9819, p. 981919.

16 C. Buurma, R. E. Pimpinella, A. J. Ciani, J. S. Feldman, C. H. Grein and P. Guyot-Sionnest, in *Optical Sensing, Imaging, and Photon Counting: Nanostructured Devices and Applications, International Society for Optics and Photonics*, 2016, vol. 9933, p. 993303.

17 A. Chu, B. Martinez, S. Ferré, V. Noguier, C. Gréboval, C. Livache, J. Qu, Y. Prado, N. Casaretto, N. Goubet, H. Cruguel, L. Dudy, M. G. Silly, G. Vincent and E. Lhuillier, *ACS Appl. Mater. Interfaces*, 2019, **11**, 33116–33123.

18 V. Pejović, E. Georgitzikis, J. Lee, I. Lieberman, D. Cheyns, P. Heremans and P. E. Malinowski, *IEEE Trans. Electron Devices*, 2021, 1–11.

19 S. Goossens, G. Navickaite, C. Monasterio, S. Gupta, J. J. Piqueras, R. Pérez, G. Burwell, I. Nikitskiy, T. Lasanta, T. Galán, E. Puma, A. Centeno, A. Pesquera, A. Zurutuza, G. Konstantatos and F. Koppens, *Nat. Photonics*, 2017, **11**, 366–371.

20 SWIR Vision, **https://www.swirvisionsystems.com**, (accessed January 28, 2022).

21 C. Gregory, A. Hilton, K. Violette and E. J. D. Klem, *SID Symp. Dig. Tech. Pap.*, 2021, **52**, 982–986.

22 S. Hinds, E. Klem, C. Gregory, A. Hilton, G. Hames and K. Violette, in *Infrared Technology and Applications XLVI*, ed. G. F. Fulop, L. Zheng, B. F. Andresen and J. L. Miller, SPIE, Online Only, United States, 2020, vol. 11407, p. 8.

23 J. Steckel, *IEEE Int. Electron Devices Meet.*, 2021, 21665864.

24 P. Malinowski, *Imaging Mach. Vis. Eur.*, 2019, 16–18.

25 E. Georgitzikis, P. E. Malinowski, Y. Li, J. Maes, L. M. Hagelsieb, S. Guerrieri, Z. Hens, P. Heremans and D. Cheyns, *IEEE Sens. J.*, 2020, **20**, 6841–6848.

26 P. E. Malinowski, J. Lee, Y. Li, E. Georgitzikis, V. Pejovic, I. Lieberman, T. Verschooten, S. Thijs, O. Furxhi, P. Heremans and D. Cheyns, in *Optical Architectures for Displays and Sensing in Augmented, Virtual, and Mixed Reality (AR, VR, MR) II*, SPIE, 2021, vol. 11765, pp. 207–212.
27 Emberion, **https://www.emberion.com/**, (accessed January 28, 2022).
28 A. J. Nozik, *Phys. E*, 2002, **14**, 115–120.
29 O. E. Semonin, J. M. Luther, S. Choi, H.-Y. Chen, J. Gao, A. J. Nozik and M. C. Beard, *Science*, 2011, **334**, 1530–1533.
30 J. Tang, K. W. Kemp, S. Hoogland, K. S. Jeong, H. Liu, L. Levina, M. Furukawa, X. Wang, R. Debnath, D. Cha, K. W. Chou, A. Fischer, A. Amassian, J. B. Asbury and E. H. Sargent, *Nat. Mater.*, 2011, **10**, 765–771.
31 C.-H. M. Chuang, P. R. Brown, V. Bulović and M. G. Bawendi, *Nat. Mater.*, 2014, **13**, 796–801.
32 M. Vafaie, J. Z. Fan, A. Morteza Najarian, O. Ouellette, L. K. Sagar, K. Bertens, B. Sun, F. P. García de Arquer and E. H. Sargent, *Matter*, 2021, **4**, 1042–1053.
33 E. Lhuillier, A. Robin, S. Ithurria, H. Aubin, B. Dubertret, E. Lhuillier, S. Ithurria and A. Robin, *Nano Lett.*, 2014, **14**, 2715–2719.
34 X. Tang, M. M. Ackerman, M. Chen and P. Guyot-Sionnest, *Nat. Photonics*, 2019, **13**, 277–282.
35 X. Tang, M. M. Ackerman and P. Guyot-Sionnest, *ACS Nano*, 2018, **12**, 7362–7370.
36 M. Chen, L. Lu, H. Yu, C. Li and N. Zhao, *Adv. Sci.*, 2021, **8**, 2101560.
37 C. Gréboval, A. Chu, D. V. Magalhaes, J. Ramade, J. Qu, P. Rastogi, A. Khalili, S.-S. Chee, H. Aubin, G. Vincent, S. Bals, C. Delerue and E. Lhuillier, *ACS Photonics*, 2021, **8**, 259–268.
38 A. Chu, C. Gréboval, N. Goubet, B. Martinez, C. Livache, J. Qu, P. Rastogi, F. A. Bresciani, Y. Prado, S. Suffit, S. Ithurria, G. Vincent and E. Lhuillier, *ACS Photonics*, 2019, **6**, 2553–2561.
39 P. Rastogi, A. Chu, T. H. Dang, Y. Prado, C. Gréboval, J. Qu, C. Dabard, A. Khalili, E. Dandeu, B. Fix, X. Z. Xu, S. Ithurria, G. Vincent, B. Gallas and E. Lhuillier, *Adv. Opt. Mater.*, 2021, **9**, 2002066.
40 X. Lan, M. Chen, M. H. Hudson, V. Kamysbayev, Y. Wang, P. Guyot-Sionnest and D. V. Talapin, *Nat. Mater.*, 2020, **19**, 323–329.
41 S. Keuleyan, E. Lhuillier and P. Guyot-Sionnest, *J. Am. Chem. Soc.*, 2011, **133**, 16422–16424.
42 B. Martinez, J. Ramade, C. Livache, N. Goubet, A. Chu, C. Gréboval, J. Qu, W. L. Watkins, L. Becerra, E. Dandeu, *et al.*, *Adv. Opt. Mater.*, 2019, **7**, 1900348.
43 A. Chu, C. Gréboval, Y. Prado, H. Majjad, C. Delerue, J.-F. Dayen, G. Vincent and E. Lhuillier, *Nat. Commun.*, 2021, **12**, 1794.
44 V. Pejović, J. Lee, E. Georgitzikis, Y. Li, J. H. Kim, I. Lieberman, P. E. Malinowski, P. Heremans and D. Cheyns, *IEEE Electron Device Lett.*, 2021, **42**, 1196–1199.
45 SWIR Vision Systems, Acuros® CQD®1920/1920L GigE SWIR Camera [Online], **https://www.swirvisionsystems.com/wp-content/uploads/Acuros-CQD-1920L-GigE-SWIR-Camera_003.pdf**, (accessed February 16, 2022).
46 M. Allen, A. Bessonov and T. Ryhänen, *SID Symp. Dig. Tech. Pap.*, 2021, **52**, 987–990.
47 J. Jean, J. Xiao, R. Nick, N. Moody, M. Nasilowski, M. Bawendi and V. Bulović, *Energy Environ. Sci.*, 2018, **11**, 2295–2305.
48 S. Zhang, M. Chen, G. Mu, J. Li, Q. Hao and X. Tang, *Adv. Mater. Technol.*, 2021, 2101132.
49 R. L. Olmon, B. Slovick, T. W. Johnson, D. Shelton, S.-H. Oh, G. D. Boreman and M. B. Raschke, *Phys. Rev. B: Condens. Matter Mater. Phys.*, 2012, **86**, 235147.
50 K. Luke, Y. Okawachi, M. R. E. Lamont, A. L. Gaeta and M. Lipson, *Opt. Lett.*, 2015, **40**, 4823–4826.
51 H. S. Dow, W. S. Kim and J. W. Lee, *AIP Adv.*, 2017, **7**, 095022.